Numerical modelling of triple-junction tectonics at Karlıova, Eastern Turkey, with implications for regional magma transport

Özgür Karaoğlu[1,2,*], John Browning[2,3], Mohsen Bazargan[2,3], Agust Gudmundsson[2]

[1]Eskişehir Osmangazi University, Department of Geological Engineering, 26040 Eskişehir, Turkey

[2]Department of Earth Sciences, Royal Holloway University of London, Egham, TW20 0EX, UK

[3]Department of Earth Sciences, University College London, Gower Street, London WC1E 6BT, UK

[*] Correspondence to: Ö. Karaoğlu, ozgur.karaoglu@deu.edu.tr; ozgur.karaoglu@rhul.ac.uk

Abstract

Few places on Earth are as tectonically active as the Karlıova region of eastern Turkey. In this region, complex interactions between the Arabian, Eurasian and Anatolian plates occur at the Karlıova Triple Junction (KTJ). The relationship between tectonics and magma propagation in triple-junction tectonic settings is poorly understood. Here we present new field and numerical results on the mechanism of magma propagation at the KTJ. We explore the effects of crustal heterogeneity and anisotropy, in particular the geometry and mechanical properties of many faults and layers, on magma propagation paths under a variety of tectonic loads. We propose that two major volcanic centres in the area, the Turnadağ volcano and the Varto caldera, are both fed by comparatively shallow magma chambers at depths of about 8 km, which, in turn, are fed by a single, much larger and deeper reservoir at about 15-18 km depth. By contrast, the nearby Özenç volcanic area is fed directly by the deeper reservoir. We present a series of two-dimensional and three-dimensional numerical models showing that the present tectonic stresses encourage magma-chamber rupture and dyke injection. The results show that inversion tectonics encourages the formation of magma

paths as potential feeder dykes. Our three-dimensional models allow us to explore the local stresses induced by complex loading conditions at the Karlıova triple junction, using an approach that can in future be applied to other similar tectonic regions. The numerical results indicate a great complexity in the potential magma (dyke) paths, resulting from local stresses generated by interaction between mechanical layers, major faults, and magma chambers. In particular, the results suggest three main controls on magma path formation and, eventual eruptions, at KTJ: (1) the geometry and attitude of the associated faults; (2) the heterogeneity and anisotropic of the crust; and (3) mechanical (stress) interactions between deep and shallow magma chambers.

Key words: triple-junction tectonics, numerical modelling, dyke propagation, Eastern Turkey

1. Introduction

One fundamental problem concerning convergent plate boundary tectonics is the nature of the interplay between deformation processes and magma transport (e.g. Hutton, 1988; Vigneresse, 1999). Networks of fractures (primarily extension fractures but also faults) and contacts play a crucial role in creating efficient paths through which magma is transported, stored and eventually erupted at the surface (e.g. Clemens and Mawer, 1992; Cembrana and Lara, 2009). Extrusion-block tectonic regimes may be characterised by triple-junction tectonics with significant components of mostly active strike-slip faulting. These regimes provide a good opportunity to understanding of the interplay between crustal stresses and magma propagation in strike-slip regimes.

A triple junction, defined as a boundary where three lithospheric plates meet, marks an important type of setting for extrusion tectonics, initiation of volcanism, and seismicity at

active plate margins. (cf. Jarosinski, 2012). Triple-junctions are the sites of abundant seismicity, high heat flow, and volcanism (e.g. Furlong and Schwartz, 2004). Although 16 types of possible triple junctions have been identified (McKenzie and Parker, 1967), the spatial and temporal relationships between magmatism and the extrusion tectonics of triple junctions remain poorly constrained. A Karlıova-type triple junction, the focus of this study, is a continental triple junction (Şengör et al., 2004) consisting of a non-subductable continental crust. Convergence is predominantly accommodated by strike-slip faults resulting in extrusion tectonics (Şengör et al., 2004).. The new data and numerical model results presented here offer excellent opportunities to clarify and constrain better the relationships between volcanism and tectonic activity at continental triple junctions.

Migration of an extruded block promotes crustal thinning of thickened accretionary complex crust composed of a variety of materials (e.g. Furlong and Schwartz, 2004). Suitably stressed crustal materials of the extruded block on the Karlıova-type triple junctions are potential regions for magma ascent. Magma in the mantle and partly in the lower crust ascends by porous flow. At shallower crustal levels, magma ascends primarily through magma-driven fractures, mostly dykes. Dyke initiation and propagation is known to be partly controlled by regional stress fields (Tibaldi, 2015), particularly those induced by crustal extension (e.g. Gudmundsson, 1990; Hurwitz, 2009; Daniels et al., 2012; Le Corvec et al., 2013; Maccaferri et al. 2014).

Magma chambers are the main sources for major polygenetic volcanoes and, partly, for associated volcanic systems, that is, swarms or fields of volcanic (and in rift zones, also tectonic) fissures and basaltic lava flows. The depths of shallow or upper-crustal magma chambers are commonly between 1 km and 6 km, particularly at divergent plate boundaries (Gudmundsson, 2012). However, some chambers reach depths of 7-9 km, depending on the tectonic regime and crustal structure, and may also be regarded as comparatively shallow

64 (Chaussard and Amelung, 2014). Chambers at greater depths are normally classified as deep-
65 seated reservoirs, and these may reach depths of 20-30 km or more (Gudmundsson, 2012;
66 Chaussard and Amelung, 2014; Le Corvec et al., 2015).

67 As is detailed below, we propose the existence of two comparatively shallow magma
68 chambers at around 8 km depth and a deep-seated reservoir at around 15 km depth in the KTJ
69 region (Figs. 1, 2). We relate these magma sources to likely magma paths, i.e dykes. For an
70 eruption to occur, the magma chamber must rupture (Browning et al., 2015) and propagate a
71 dyke or an inclined sheet to the surface (Gudmundsson, 2012; Chestler and Grosfils, 2013; Le
72 Corvec et al., 2013; Caricchi et al., 2014). The conditions for magma-chamber rupture and
73 dyke injection have been analysed by many (e.g. Gudmundsson, 1990, 2006; Grosfils, 2007;
74 Hurwitz et al., 2009; Gerbault, 2012; Le Corvec et al., 2015). Many of the basic ideas are
75 reviewed and analysed by Gudmundsson (2012), with particular reference to direct
76 observations of fossil magma chambers and the results of hydraulic fracture stress
77 measurements in drill-holes worldwide down to crustal depths of about 9 km.

78 Generally, the critical stress required for magma-chamber rupture can be reached in
79 two ways (Gudmundsson, 1990, 2006; Folch and Marti, 1998; Browning et al., 2015): (1) by
80 increasing the total pressure inside the chamber (for example, by adding magma to the
81 chamber or through gas exsolution from its magma), and (2) by external extension, such as in
82 rift zones, where divergent plate movements gradually reduce the minimum principal
83 compressive stress σ_3. Tensile fractures do not normally extend to depths greater than 0.5-1
84 km. If they try to propagate to greater depths they will change into closed normal faults, in
85 accordance with Griffith criterion (Gudmundsson, 2011). There are thus no open tension
86 fractures or open normal faults at the depth of many kilometres ready to be filled with magma
87 to form dyke fractures. By contrast, dyke fractures are initiated when the excess pressure in
88 the chamber reaches the host-rock tensile strength under either loading condition. Then the

89 magma chamber ruptures and a dyke (or an inclined sheet) is injected (Gudmundsson, 1990;
90 Gaffney et al., 2007). The mechanical layering and local state of stress inside the volcano,
91 together with rate of magma solidification and other factors, ultimately determine whether the
92 dyke propagates to the surface and erupts or, alternatively, becomes arrested at depth in the
93 volcano (e.g. Spence et al., 1987; Gudmundsson, 1990, 2011; Acocella and Neri, 2009; Geshi
94 and Neri, 2014).

95 Although the geometries of magma chambers vary, many and perhaps most crustal
96 magma chambers are sill-like (Gudmundsson, 1990; Annen and Sparks, 2002; Kavanagh et
97 al., 2006; Grosfils et al., 2015) as evidenced by seismic studies of volcanoes and rift zones
98 (Sinton and Detrick, 1992) and field studies of fossil chambers, that is, plutons (Pasquarè and
99 Tibaldi, 2007; Tibaldi et al., 2008; Gudmundsson, 2012). Numerical, analogue, and field
100 studies indicate that piston-type calderas are often associated with a sill-like magma
101 chambers (Geyer et al., 2006; Geyer and Marti, 2009; Gerbault, 2012; Gregg et al., 2012,
102 2015; Le Corvec et al., 2013; Gudmundsson, 2015). The size of an underlying shallow
103 magma chamber is then thought to closely resemble the radius of associated collapse caldera,
104 whereas the deeper reservoirs may be many times larger (Gudmundsson, 2012, 2015;
105 Grebault, 2012; Gregg et al., 2013; Grosfils, 2007, 2015; Browning and Gudmundsson,
106 2015). As indicated above, the depths of many magma chambers have been estimated using
107 petrological, geochemical, and geophysical methods (Becerril et al., 2013; Chaussard and
108 Amelung, 2014).

109 The emplacement of hot asthenospheric mantle to shallow levels beneath a Karlıova-
110 type triple junction could be expected to generate melt and, likely, surface volcanism.
111 Consistent with this expectation is the sequence of volcanic centres that have erupted in the

112 wake of the triple junction within the Karlıova regime (e.g. Furlong and Schwartz, 2004;
113 Gaffney et al., 2007).

114 This study focuses on the mechanism of magma propagation, primarily through
115 dykes, in the Karlıova Triple Junction (KTJ) tectonic regime. We aim to demonstrate how
116 fault geometry and mechanical properties may affect magma propagation under a variety of
117 tectonic boundary loads. We discuss the geologic setting of the KTJ and the manifestations of
118 shallow and deeper magma chambers within the crustal segment. Our numerical modelling
119 aims to quantify the crustal response to various tectonic regimes in Eastern Turkey. The
120 region is characterised by considerable lithological heterogeneity and anisotropy (cf.
121 Jarosinski, 2012) which are taken into account in our numerical models. We present a series
122 of two-dimensional and three-dimensional numerical models to help constrain evolving ideas
123 regarding the tectonics of the KTJ. We also analyse a north-south striking profile that is
124 subject to regional compression and local extensional tectonic phases which likely operated
125 in the region ~3 My. A general three-dimensional model is presented to show the local stress
126 effects resulting from complex regional loading on crustal magma chambers.

127 **2. Geologic and tectonic setting**

128 Eastern Turkey is a part of the Mediterranean region which is characterised by the
129 presence of major continental fragments and suture zones (Şengör et al., 2004). Propagation
130 of the westward extrusion of the Anatolian block, just after the formation of the Northern
131 Anatolian Fault Zone (NAFZ), started around 12 Ma from the pivot point of KTJ and
132 triggered lithosphere-scale transtensional deformation (Barka, 1992; Şengör et al., 2004). The
133 NAFZ, whose main fault is the active right-lateral North Anatolian Fault (NAF), is a nearly
134 2000 km long zone, extending from Karlıova in eastern Anatolia to the tip of the Corinth Rift

in Greece (Armijo et al., 1999). The overall width of NAFZ increases from ~10 km (Figs. 1, 2) in the east to ~100 km in the west (Şengör et al., 2004).

Present-day earthquake focal-mechanism solutions indicate dextral transtensional movements (McKenzie, 1972; Ozener et al., 2010) on the Yedisu Fault at the western part of the KTJ (Fig. 1). GPS data show that the eastern part of the Anatolian plate (the western part of the KTJ) moves at a rate of ~20 mm/yr with respect to the Eurasian plate (Fig.1, McClusky et al., 2000; Reilinger et al., 2006). Solid-block modelling of the region and GPS velocity data (Fig. 1) show that eastern margin of the KTJ is undergoing crustal shortening, whereas in the west the prevailing tectonic stress and crustal deformation is transtensional to the west (Barka, 1992; Aktug et al., 2013). The present geodetic average slip rate for Eastern Anatolian Fault Zone (EAFZ) is 5 mm/yr (Aktug et al., 2013). The EAFZ is around 30-km-wide at the eastern extremity near the KTJ. It is proposed that the fault zone has been active since the Pliocene (Tatar et al., 2004).

The NAFZ and EAFZ, which are two western branches of the KTJ, are characterised by transtensional tectonics (Şengör et al., 2004). The right-lateral Yedisu Fault (YS, Fig. 1), striking N105°E, represents the eastern branch of the NAFZ and extends for more than 30 km to the KTJ (Fig. 1). The VFZ extends for over 50 km, strikes N105°E-N120°E and can be subdivided into six fault segments (Sançar et al., 2015). The Varto Fault (VF, Fig. 2c) is seismically the most active segment of the VFZ; it is a N120°E-striking right-lateral strike-slip fault with a reverse component that offsets the southern part of the Varto caldera. Two destructive earthquakes (Mw = 6.8 and 6.2) occurred on the VFZ in 1966 (Fig. 2c, Ambraseys and Zatopek, 1968). Karaoğlu et al. (in press) suggest that the combined motions of NW-striking dextral, normal, oblique and thrust faults indicate a successive and reactive

158 tectonic phase that caused incremental complex movement of numerous fault blocks during
159 the deformation of the Karlıova and Varto region since 6 Ma.

160 Structural and stress data indicate a distinct kinematic behaviour of the KTJ during
161 the past 12 Ma (Şengör et al., 2004). Following the formation of NAFZ and EAFZ, the
162 western part of the triple junction has been subject to transtensional tectonics during which
163 the east end of the KTJ has undergone incremental deformation accommodated by numerous
164 faults during (i) ongoing shortening phases driven by the regional-scale thrust tectonic regime
165 and (ii) transtensional phase caused by westward extrusion tectonics at a local-scale
166 (Karaoğlu et al., in press). It has been suggested that a right-lateral motion developed under a
167 NE–SW-trending extension associated with NW–SE contraction. The fault surface planes of
168 the WNW–ESE-striking VFZ were reactivated at 3 Ma, which suggests that inversion
169 tectonics occurred when transtensional faults reversed their movement during a subsequent
170 compressional tectonic episode (e.g. Williams et al., 1989). Since 3 Ma, thrusting shifted
171 further south, coupled with a component of dextral strike-slip motion (Karaoğlu et al., in
172 press).

173 Volcanic activity commenced on the EAF with some eruptions producing acidic rocks
174 whose ages are between 4.4 and 6.06 Ma (Poidevin et al., 1998). The earliest volcanism
175 occurred at around 6 Ma and highlights the initiation of crustal deformation in the EAF. As
176 for the deformation of Varto and Turnadağ volcanoes, the age of the basement volcanic rocks
177 in the southern part of Varto is around 3 Ma (Fig. 2a). The lifespan of the Varto caldera
178 volcanism is estimated at between 3 and 1 Ma (Hubert-Ferrari et al., 2009). This may be
179 regarded as the second major volcanic episode in the area. The third event or activity in the
180 area relates to some small-scale volcanism on the southern sector of the VFZ. The resulting
181 domes are dated at approximately 0.73 Ma to 0.46 Ma (Fig. 2a). The most recent dyke-fed

182 eruptive and effusive-type volcanism (1.96-2.67 Ma, based on K/Ar ages from Biggazi et al.
183 1997, 1998) occurred around the Özenç area, at the southern part of the Varto caldera (Fig.
184 2). The volcanism produced partly mafic lavas, mostly of the alkaline and rarely sub-alkaline
185 series, including basaltic trachy-andesite and basaltic andesite (Buket and Temel, 1998;
186 Hubert-Ferrari et al., 2009). The Varto caldera, the Turnadağ volcano, and the Özenç
187 volcanic area (Fig. 2) show distinct volcanic facies, and also certain geochemical
188 characteristics (e.g. Buket and Temel, 1998; Hubert-Ferrari et al., 2009; Sançar et al., 2015).

189 **3. Magma-chamber geometry**

190 In order to estimate the rough geometry and depth of the magma chamber feeding a
191 polygenetic volcano, field and analytical data are required. There have not, however, been
192 any petrological or geodetic studies on the geometry of the magma feeding systems in
193 Eastern Turkey. Recent compilations, based on various methods, suggest that most magma-
194 chamber or reservoir depths worldwide range from about 1 km to about 20 km below the
195 volcanoes to which they supply magma (Middlemost, 1997; Gudmundsson, 2012; Chaussard
196 and Amelung, 2014; Tibaldi, 2015). The exact depths of the magma chambers for the
197 volcanoes Turnadağ and Varto (Fig. 2b), as well as for the Özenç volcanic area, are not
198 known. The chemistry of the eruptive materials suggest that the source chamber for the
199 Özenç volcanism is deeper and larger than the chambers beneath Turnadağ and Varto. All
200 these areas, however, contain dykes whose aspect (length/thickness) ratios can be used to
201 estimate the depths of the source chambers.

202 We use a method based on the principles of fracture mechanics and fluid-dynamics to
203 constrain the depth of the magma chambers/reservoirs at Karlıova (e.g. Becerril et al., 2013).
204 All dykes in the area are dominantly trachy-basaltic in composition. Magma overpressure (p_o)
205 within a dyke during its formation can be estimated from the ratio of dyke strike dimension

206 (L) and thickness (Δu_I). A total of 14 dyke measurements in the study area were used to
207 estimate their depth of the source chamber/reservoir. The method is as follows. The opening
208 displacement of an elastic mode I (tensile mode) crack, such as a dyke, subject to internal
209 fluid or magma overpressure (driving pressure) p_o is given by:

210 $$\Delta u_I = \frac{2p_o(1-\nu^2)L}{E} \quad (1)$$

211 where L is the smaller of the strike and dip dimensions of the fracture, and E and ν are
212 Young's modulus and Poisson's ratio, respectively, of the host rock. While Δu_I denotes the
213 opening or aperture of the dyke at its time of emplacement it also corresponds roughly to the
214 thickness of a solidified dyke as measured in the field (the error due to contraction as the
215 magma as the dyke solidifies is about 10% - Becerril et al., 2013). Here we use 40 GPa as an
216 average Young's modulus for the host rock and 0.25 for the Poisson's ratio. The overpressure
217 in a dyke at the crustal level of exposure (at the surface for a feeder) is given by

218 $$p_o = p_e + (\rho_r - \rho_m)gh + \sigma_d \quad (2)$$

219 where p_e is the fluid excess pressure in the source magma chamber, ρ_r is the average density
220 of the host rock, ρ_m is the average density of the magma in the dyke, g is acceleration due to
221 gravity, h is the dip-dimension or height of the dyke, and σ_d is the differential stress (the
222 difference between the vertical stress and the minimum principal horizontal stress) at the
223 depth in the crust where the dyke is measured or, for a feeder-dyke, the stress difference at
224 the surface where the volcanic fissure forms. From equations (1) and (2) the depth to the
225 intersection between the source magma chamber and the feeder dyke is:

226 $$h = \frac{\Delta u_I E}{2L(1-\nu^2)(\rho_r - \rho_m)g} - \frac{p_e + \sigma_d}{(\rho_r - \rho_m)} \quad (3)$$

227 Using Eq. (3), we calculated the depth to the source of the feeder-dykes exposed in
228 the three volcanic regions under consideration (Fig. 1). We use the typical trachy-basaltic
229 magma density (ρ_m) of 2730 kg. m^{-3} (e.g. Middlemost, 1997). Since there are no detailed and
230 accurate density data for the crust of the Eastern Anatolia Accretionary Complex, we have
231 used a revised geological stratigraphy made of 18 lithologic units (Appendix 1), of the region
232 (e.g. Tarhan, 1991). The crust is thought to be mostly composed of units of limestone,
233 metamorphic rocks, massive gabbro and sandstone with estimated laboratory densities in the
234 range from about 2000–3100 kg m^{-3} (e.g. Gudmundsson, 2011). We use an average density of
235 2650 kg. m^{-3}. Note that excess magma pressure in the chamber/reservoir (p_e) is defined as
236 pressure in excess of lithostatic stress or pressure and thus automatically takes into account
237 the effects of gravitational loading (e.g. Gudmundsson, 2011, 2012).

238 The measured feeder-dyke thicknesses range from 0.8 to 3 m. The estimated
239 overpressures from Eq. (1) are from 9 to 11 MPa for the Varto and Turnadağ volcanoes and
240 from 15 to 18 MPa for the Özenç volcanic area (flood basalts). These are similar
241 overpressures as estimated for dykes in many other areas (e.g., Becerril et al., 2013). Using
242 these and the above values, Eq. (3) yields source-chamber depths of 8–10 km for Varto and
243 Turnadağ volcanoes, and 15-18 km for the Özenç volcanic area (Appendix 2). In the
244 numerical models we thus use an estimated depth of 8 km for the magma chambers feeding
245 eruptions in volcanoes of Varto and Turnadağ and 15 km for the larger reservoir supplying
246 magma to the flood basalts of the Özenç volcanic area.

247 **4. Model set-up**

248 All the numerical models are built and solved using the finite element program
249 COMSOL (www.comsol.com; cf. Zienkiewicz, 1979; Deb, 2006; Tabatabaian, 2014). The
250 models are based on the real geological setting of the KTJ as interpreted from field

measurements and seismic data (e.g. Sandvol et al., 2003) as well as InSAR data (Cavalié and Jónsson, 2014). We differentiate between two predominant magma-chamber modelling techniques. The first uses 2-D geometry where magma chambers are modelled as holes with applied excess pressure (p_e) (Gudmundsson, 2006, 2011; Gerbault, 2012; Gerbault, 2012). The second set uses 3-D geometry where the chambers/reservoirs are modelled as ellipsoids of prescribed volume with applied excess pressure. We present two geometries of 2-D models based upon (1) a N-S striking profile through the Varto caldera (Fig. 2), and (2) an E-W striking profile that encompasses both the Turnadağ volcano to the west and the Varto caldera to the east.

Our models consider ellipsoidal magma chambers/reservoirs. While these are, in detail, simplifications of the actual shapes, the long-term stable geometries may be similar to these (e.g. Gudmundsson, 2012). Topography may affect near-surface stress fields. However, in the present models the primary focus is on the local stresses induced by the stress concentration around chambers/reservoirs subject to different boundary conditions, in which case topography normally plays a less prominent role (cf. Gaffney and Damianac, 2006; Gudmundsson, 2006). Thus, we assume a flat topography in all models. The 16 different mechanical layers used in our models are based on our direct geological observations. The values used to calculate magma chamber depth encompass all of these mechanical layers.

In Fig. 3 we show only the N-S model setup. In this model two magma chambers, one relatively shallow, at a depth of 8 km, and one deeper, at a depth of 15 km, are residing within a heterogeneous, anisotropic elastic half space with Young's modulus (E) varying between individual layers from 40 GPa to 0.1 GPa, as shown in Fig. 2. The shallower magma chamber has a maximum diameter of 9 km, whereas the deeper chamber or reservoir has a maximum diameter of 30 km. Poisson's ratio (ν) does not vary significantly between

individual layers; thus, in the models we use a constant typical value for rocks of 0.25 (Gudmundsson, 2011). In the N-S striking profile all the layers dip gently to the north, whereas the E-W striking profile hosts predominantly horizontal layers. The softest (most compliant) layers are those comprising the fault cores/damage zones (E_{fault}), indicated by black polygons in Fig. 3. The faults are given Young's modulus values of 0.1 GPa, as has been estimated for some active faults (Gaffney et al., 2007; Gudmundsson, 2011; Grosfils et al., 2015). The thicknesses of layers and fault cores/damage zones are taken from our geological measurements (Fig. 2) and given in Appendix 1. All 2-D models are fixed at the corners, with boundary loads applied at the left and right edges and a free surface (a region free from shear stress) prescribed on the upper edge. More specifically, the fixing of the models at the corners means that the model boundaries are free to move (be displaced) under loading, except for the corners themselves. This is a standard procedure in modelling magma chambers subject to various loading conditions (e.g. Gudmundsson, 2006, 2011).

Loading conditions applied are (1) internal magmatic excess pressure between 5 and 15 MPa, (2) regional extension (tension) of 5 MPa, (3) regional compression of 5 MPa, and (4) a combination of regional stress and magmatic excess pressure. Magma-chamber rupture and dyke injection is supposed to occur when the tensile stress, mostly measured through hydraulic fracturing and down to crustal depths of about 9 km, are between 0.5 and 9 MPa, the most common values being 2-4 MPa (Gudmundsson, 2011). As indicated above, by using excess pressure in the chamber/reservoir, rather than total pressure, the effects of gravity are automatically considered (cf. Gudmundsson, 2012). We use a triangular mesh with a maximum element size of 4.02 km; minimum element size of 0.018 km for 2-D, and tetrahedral mesh with a maximum element size of 4.02 km; minimum element size of 1.8 km for 3-D models.

Due to the complex tectonic nature of a triple junction it is not possible to fully encompass the regional stress pattern in two dimensions. For this reason we made additional 3-D models that allow more boundary loading options. In contrast to the two-dimensional models, in these 3-D models results can be observed normal to the plane of interest. In the 3-D models, we impose three magma chambers of similar depths and sizes to those used in the 2-D models, i.e, two shallow chambers at 8 km depth and one deeper and larger reservoir at 15 km depth. The axes (diameters) of the ellipsoidal shallow chambers are 2 km, 6 km, and 9 km (Fig. 2b), similar in general dimensions to many shallow magma chambers (Gudmundsson, 2012). By contrast, the axes of the 4 km, 12 km, and 30 km (Fig. 2b), and thus similar in geometry and dimensions to many inferred deep-seated reservoirs in rift zones (Gudmundsson, 1990, 2006). All 3-D models simulate an elastic half space with a Young's modulus of 40 GPa. In these models the focus is not on the mechanical contrast between individual layers but on the effect of regional stresses on spatial distribution of the local stresses around the magma chambers. The boundary loads prescribed in these 3-D models include (1) compression or extension various directions in relation to the axes of the magma chambers/reservoirs had (2) shear, that is, compression or extension in opposing directions across a zone, thereby simulating strike-slip tectonics.

5. Results

In order to characterise the propagation path of dykes in the shallow crust at the KTJ it is first necessary to consider the stress required for magma chamber rupture. In the simplest terms, a magma chamber will rupture and inject a dyke or an inclined sheet when (Gudmundsson, 1990, 2011):

$$p_l + p_e = \sigma_3 + T_o \qquad (4)$$

where p_l is lithostatic pressure and p_e is the excess pressure in the magma chamber, σ_3 is minimum principal compressive stress in the host rock, and T_o is the tensile strength of the host rock which, as indicated above, ranges from 0.5 to 9 MPa (cf. Amadei and Stephenson, 1997). When a chamber roof has failed in tension and a dyke is initiated then the magma follows the path or trajectories of maximum principal compressive stress, σ_1 (Gudmundsson, 2011).

5.1 Magma-chamber excess pressure

Here we present first the results on crustal stresses induced solely by magmatic excess pressure within each chamber, ignoring initially the potential effects of any regional tectonic loading. In Fig. 4 we show the magnitudes of the minimum principal compressive (maximum tensile), stress, σ_3, and von Mises shear stress, τ. In both the N-S and E-W profiles the maximum tensile and shear stresses concentrate at the lateral margins of each magma chamber and at the earth's surface above the magma chamber. Complex stress patterns and interactions occur at depth because of the attitude and mechanical properties of the imposed fault structures. In all models the soft or compliant material that comprises each fault zone inhibits stresses within the fault, but raises and concentrates stresses at the boundaries or contacts of the faults with the host rock. The effects are, for example, prominent in the steeply dipping East Anatolian Fault (EAF) segment that extends between the shallow and deep chambers along the E-W profile (Figs. 4a, b). At this location (Fig. 4a) high shear stresses concentrate where the fault zone intersects the surface and at depth high tensile stresses occur where the fault zone narrows (Fig. 4c). In the N-S profile, two shallow dipping faults concentrate both shear and tensile stress between the margins of the deep and shallow chambers, indicating that magma transfer between the two systems in this location is likely (Figs. 4a, b). Stress also concentrates at depth along the EAF in the E-W profile (Figs. 4c, d).

346 It should be noted that we did test excess magmatic pressure of 15 MPa (and 10 MPa
347 as well) for the loading of the magma chambers/reservoirs. However, in the models presented
348 here we used only 5 MPa as the loading, both as regards the magmatic excess pressure as
349 well as for the external tension (in some of the models). This we did primarily because 5 MPa
350 is similar to the in situ tensile strength of rocks. Increasing the excess magmatic pressure
351 simply increases the stress concentration magnitudes (higher stresses close to the chamber, in
352 particular) but does not markedly change the geometry of the concentration zones and their
353 location – as is well known from numerical modelling in volcanology and other fields (e.g.
354 Gudmundsson, 2011).

355 ***5.2 Regional tectonic stresses***

356 In the second set of 2-D models the focus is on the effect of regional stresses induced
357 by tectonic loading on the local stresses around the magma chambers. In Fig. 5 we show the
358 tensile and shear stresses around overpressured magma chambers subjected to both regional
359 compression and regional extension, as indicated by arrows in the Fig. 5. During E-W
360 extension of 5 MPa, two stiff (high Young's modulus) near-surface units concentrate tensile
361 stress, which may encourage dyke propagation (Gudmundsson, 2006). Focussing on the EAF
362 (Figs. 5e-h), we note that shear stress concentrates at the surface during regional compression
363 but dissipates during imposed regional extension in both strike directions (Figs. 5a, e). The
364 N-S striking profile is dominated by a series of high angle faults (Fig. 5a) that during regional
365 compression (Figs. 5a-d) suppress much of the shear stress surrounding the deeper chamber
366 (Figs. 4b, 5d). The effect is similar during regional extension; however, the steepest central
367 fault concentrates substantial shear stress directly above the central part of the deep chamber.
368 Our models also show that caldera-related ring faults increase the maximum tensile stresses
369 (Figs. 5a, c).

370 Regional tectonic loading gives different stresses which potentially affects magma
371 paths. The effect is most clear in the E-W profile whereby tensile stresses are shifted to the
372 west at the Turnadağ volcano during regional extension. Our findings also indicate an
373 increased likelihood of shallow chamber dyke injection from the deeper source during
374 periods of regional extension.

375 ***5.3. Three-dimensional models***

376 In order to better understand the geodynamic setting of the Karlıova Triple-Junction
377 we present a series of simple three-dimensional (3-D) models (Figs. 6-10) exploring the local
378 stresses in differential tectonic regimes. These models are homogeneous; the aim here is not
379 to fully encompass the geological setting of Karlıova but instead to provide constraints on the
380 location of volcanism as a function of different tectonic loading. In Figs. 6a, b in the E-W
381 profile we apply a north-south directional extensional load of 5 MPa and observe the resultant
382 tensile and shear stresses along E-W and N-S profiles. The deeper and shallower chambers
383 concentrate shear stress at their margins. However, those shear stresses dissipate close to the
384 surface, and then the stress state is dominated by the deeper chamber at Earth's free surface
385 (Figs. 6a-d). Maximum tensile stresses concentrate at the lateral margins of all the chambers,
386 which suggests that the chamber walls tend to rupture and dykes become injected at these
387 locations (Figs. 5a-b).

388 In Figs. 7, 8 and 9, we model the loading effects of strike-slip faulting, using
389 compressional load of 5 MPa on either side of the N-S-striking plane (Fig. 7). Such a regime
390 cannot be represented fully in a two-dimensional model. As in previous models we show the
391 magnitudes of tensile and shear stresses, although now in two directions (Figs. 7-9). We note
392 stress concentrations and linkage between the deeper chamber and the shallow chamber
393 directly above (Varto) (Fig. 7). Surface stresses are dominated by the larger reservoir, and no

stress interaction occurs with either chamber or the shallow chamber to the west (Figs. 7b, d). There are tensile stress concentrations around, and particularly above and in-between, the chambers and reservoirs of Varto and Özenç (Fig. 7c). This stress concentration between the chamber and the reservoir may promote rupture at the upper margin (the roof) of the reservoir and encourage dyke propagation from the reservoir to the shallow chamber. Furthermore, from the shallow chamber there is a zone of tensile stress concentration all the way to the surface (Fig. 7a), suggesting that the local stress field encourages dyke propagation from the chamber to the surface. While these models only show the stress magnitudes, we also analysed the stress trajectories (the directions of the principal stresses) and these agree with the suggested dyke paths.

We also made a set of three-dimensional models to explore the effect of N-S and E-W directed regional extension. Even though these models do not accurately reflect the exact tectonic regime of the study area, the results are general and should broadly apply to triple junctions worldwide, even regions where biaxial tension might operate (Appendix 3). We note again that there is very little stress interaction between the eastern and western magmatic systems. Whilst magma propagation between the two systems is unlikely, it appears substantially more difficult to envisage linkage or interaction during a compressional regime where tensile stresses are lower in the area between the eastern and western chambers. In the eastern segment, our results indicate an increased likelihood of magma chamber rupture at the lateral margin of each chamber during extensional loading. We find that extensional loading favours central chamber roof rupture and vertical dyke propagation. As indicated in our earlier models (Figs. 5a, e), the precise direction of the dyke propagation path will depend on local stresses related to crustal heterogeneity and anisotropy (layering). However, the extension appears to have shifted the principal stresses towards the north in comparison to the previous models that consider only extension or compression independently.

In Figs. 8 and 9 we compare the effects different types of shear, that is, left-lateral and right-lateral strike-slip faulting, on the local stresses, particularly around the magma chambers/reservoirs. The main finding is that the shear and tensile stresses again concentrate around the chambers/reservoirs, but the stresses concentrated around the deep-seated chamber (reservoir) are greater at the surface in the right-lateral simulations (than in the left-lateral simulations, shifting stresses slightly to the east (Fig. 9c). In Fig. 10 we simulate a N-S compressional regime which has the effect of increasing the symmetry of local stresses, and in doing so concentrating both tensile and shear stresses vertically above the deeper magma reservoir.

6. Discussion

Over the past decades many studies have focused on understanding better the mechanical principles that control dyke propagation paths through the Earth`s crust (e.g. Druitt and Sparks, 1984; Martí et al., 1994; Acocella et al., 2004; Geyer et al., 2006; Gudmundsson, 2006; Martí et al., 2008; Hurwitz, 2009; Gerbault, 2012; Gudmundsson, 2012; Le Corvec et al., 2013; Karaoğlu, 2014). Although some studies have attempted to understand how faults affect magma ascent (Magee et al., 2014; Browning and Gudmundsson, 2015; Gudmundsson, 2015) many aspects of fault-magma path interactions remain poorly understood. Our work focuses on the mechanism of dyke propagation through a highly heterogeneous, anisotropic, and intensely faulted crust of the KTJ. It is widely accepted that the region has experienced N-S directed crustal shortening. We have also taken into consideration the inversional tectonic regime, i.e., a successive N-S directed extension and compression during the past 3 Ma, an idea based on the results of recent field studies (Karaoğlu et al., in press). We further accounted for dyke propagation under either E-W compressional, or E-W extensional tectonic regimes (Fig. 4), as well as strike-slip regimes.

443 The numerical results presented demonstrate that the initiation of a dyke is influenced
444 by the geometries and depths of magma chambers as well as the local stresses in the
445 heterogeneous, anisotropic, and faulted crust. The overall process of dyke initiation and
446 propagation may be affected by at least three distinct factors, namely (i) the geometry and
447 attitude of the associated faults; (ii) the heterogeneity and anisotropy of the crust; and (iii)
448 stress concentrations around, and stress (mechanical) interactions between, magma chambers.
449 Here we discuss our numerical analysis of two different tectonic regimes, namely inversion
450 tectonics using N-S and E-W-striking profiles in order to better understand dyke propagation
451 under different stress conditions at the Karlıova-Varto region.

452 ***6.1 Magma transport in the absence of tectonic stresses***

453 Our numerical models indicate that the mechanical properties of a heterogeneous and
454 anisotropic crust substantially influence the local stresses and thus the potential dyke
455 propagation paths (e.g. Chaussard and Amelung, 2014; Le Corvec et al. 2015) (Fig. 4). The
456 initial stage of dyke propagation is magma-chamber roof rupture leading to the initiation of a
457 dyke (e.g. Clements and Mawer, 1992; Gerbault, 2012). One of the most common reasons for
458 the generation of excess pressure within a shallow magma chamber is likely recharge from
459 parental magma at depth that has accumulated in a deeper reservoir or chamber (e.g. Chestler
460 and Grosfils, 2013). It is only when a sufficient volume of magma accumulates within a
461 shallow chamber that it can reach the conditions of likely rupture (Eq. 4; Browning et al.,
462 2015). Dyke propagation at great depths requires suitable stress interactions between the
463 shallower and the deeper magma chambers or reservoirs (Fig. 4a). Our numerical results
464 show that layering affects local stresses and many aspects of fault-dyke path interactions
465 (Figs. 4c, d). For all loadings considered (compression, extension, and shear), tensile and

466 shear stresses concentrate around, and particularly at the margins of the deep magma
467 chambers (Fig. 4).

468 While the 4 km wide EAF is one of the most remarkable structural elements along the
469 E-W profile (Fig. 4c), the conditions for dyke propagation through and along a fault are only
470 observed at the much smaller VFZ primarily due to the faults orientation and position.
471 However, we note some minor stress accumulation in the EAF (Figs. 4c, d). Tensile stress
472 along the VFZ likely creates favourable conditions for dyke propagation along the previously
473 dissected fault at the northern margin of the deeper reservoir. This result suggests that deep
474 and shallow magma chamber stress interactions may play an important role in dyke
475 propagation which is strongly influenced by faults and other crustal heterogeneities and
476 layering (Fig. 4).

477 ***6.2 Magma transport under regional tectonic stresses***

478 Magmatic systems evolve partly as a result of tectonic deformation, generally and in
479 the context of processes associated with the KTJ. Recently, this area has experienced N-S
480 directed compression and E-W directed extension (e.g. Aktug et al. 2013). In the E-W profile,
481 shallow dyke injection, some reaching the surface to erupt, appears possible during both
482 extensional and compressional tectonic loading in and around the Varto caldera (Figs. 5e, g).
483 Deep and shallow magma chamber interactions may result in magmatism that becomes partly
484 channelised through the EAF, thereby encouraging volcanic eruptions in the Varto region.
485 Our results demonstrate that fault zones may facilitate magma transport during different
486 tectonic loadings. The effects of these faults on potential magma paths is more prominent for
487 compressional (Figs. 5g, h) than extensional loading (Figs. 5e, f).

488 While tensile and shear stresses concentrate mostly at the margins of the shallow
489 magma chambers, shear stresses concentrate also above the central parts of the deeper

chambers/reservoirs (Fig. 5h), as well as at caldera ring-faults (e.g. Annen and Sparks, 2002; Marti et al., 1994). Our models indicate how magma transport and regional tectonics may interact in an intensely fragmented and mechanically layered crust (e.g. Spence et al. 1987; Tibaldi et al., 2008), in particular through the cross faults of the VFZ (Figs. 5b, d). The vertical stress patterns between the two magma chambers observed in the N-S profile support the view that fault zones can act as magmatic paths (Fig. 5d). Even during a N-S compressional phase the results suggest that dykes may be injected, resulting in possible dyke injection from the deeper source to the shallow magma chamber (Fig. 5d). In the case of N-S extension (Fig. 6), the youngest fault, which is a normal fault as shown in Fig. 2a, plays a crucial role for shear stress concentration (Figs. 5a-d and Fig. 6). We show that the interaction between these fault systems, of various ages, encourages dyke injection from the central part of a deeper magma reservoir, and therefore acts as a potential vertical dyke path (Fig. 5b).

6.3. Numerical models in the Karlıova geological context

In the 2-D models, Varto caldera is represented by steeply dipping inward zones of soft material, as is commonly observed in eroded ring-faults of calderas (e.g. Marti et al. 2008; Browning and Gudmundsson, 2015). The Varto caldera is 8 km in diameter and with a semi-circular shape. The Varto fault is the most seismically active segment of the VFZ, a N70°W-striking fault that offsets the southern part of the Varto caldera (Fig. 1). Several distinct dyke locations have previously been reported, the dykes being primarily composed of trachy-basalt, both inside and around the Varto caldera. Those dykes mostly display NW–SE, and rarely NE–SW, orientations. Strike orientation values range from 205° to 300° with some indicating the presence of cross-cutting (polyphase) dykes. Our numerical results indicate the potential for multi-stage dyke injections during transtensional to compressional tectonic

514 phases (e.g. inversion tectonic regime) resulting principal stress rotation (Fig. 5). Although
515 radiometric data of Varto caldera yields ages from 3.1 to 2.6 Ma (Hubert-Ferrari et al., 2009),
516 which might represent the duration of the volcanism, magma propagation in the crust has
517 probably continued up to the latest eruptions, based on our numerical results (Fig. 5). Recent
518 block rotations around the KTJ based on GPS data (Fig. 1) indicate an intense crustal
519 deformation via successive extensional and shear loading (e.g., Le Corvec et al., 2013; 2015).
520 Long-lived volcanic activity is possible at Varto caldera and in the KTJ in general.

521 Zones of tensile stress concentration indicate potential magma propagation paths from
522 the shallow magma chambers to the surface of Turnadağ volcano (Fig. 5e). Magma transfer
523 under E-W-oriented compression is unlikely (Figs. 5g, h). Dyke-fed eruptions at Turnadağ
524 volcano are most likely when the magma chamber feeding the volcano is subject to an E-W-
525 directed extension (Fig. 5e). On account of the westward extrusion of the Anatolian plate
526 since 12 Ma, an E-W-directed tectonic regime seems most favourable for eruptions in the
527 Turnadağ volcano (Figs. 1, 5e).

528 In the Özenç volcanic area our numerical models suggest that volcanic activity is
529 more likely under E-W-directed extension than N-S-directed extension, and may occur under
530 E-W-directed compression as well. We indicate that some, perhaps most, of the feeder dykes
531 may have originated from the deeper magma chamber (Figs. 5c, d). In particular, 3-D
532 modelling results suggest that the deeper magma chamber largely controls the local stress
533 field and, thereby, dyke propagation and resultant eruptions (Figs. 7, 8, 9).

534 Our 3-D models show the potential for subtle changes in magma propagation paths
535 and eventual eruption resulting from the differences in the boundary loads. While all-round
536 extension has the likely effect of shifting volcanism to the south-east (Appendix 3), strike-slip
537 type loading can either concentrate volcanism directly above a deep magma system or extend

538 the zone of volcanism substantially to the east, depending on the loading direction (Figs. 7, 8,
539 9). All results show that the most likely paths for dyke propagation to the surface are from the
540 eastern margin of either the deeper chamber or, possibly, the eastern margin of the shallow
541 (Varto) chamber.

542 ***6.4. Relationships between local stress fields in Karlıova and volcanic eruptions***

543 Studies indicate that most volcanic unrest periods do not culminate in an eruption
544 (Dzurisin, 1991). Only during comparatively rare periods do dykes propagate all the way to
545 the surface and erupt. For eruptions to occur, the local stresses between the source and the
546 surface along the potential dyke path must be uniform, that is, homogenised (Gudmundsson
547 and Philipp, 2006).

548 Crustal heterogeneity and anisotropy as well as fault attitude and mechanical
549 properties are the main parameters which influence the local stresses and thereby the magma
550 paths (e.g. Gudmundsson and Philipp, 2006; Browning and Gudmundsson, 2015). Our
551 models suggest that, for many loadings, regional tectonic stresses encourage dyke
552 propagation to the surface.

553 Since the development of the NAFZ and EAFZ, at around 6 Ma, a strike-slip tectonic
554 regime has dominated the province. Westward extrusion of the Anatolian plate led to a stress
555 field suitable for magmatism at the extremity of the KTJ. The wedge extrusion
556 accommodated by high strain encouraged magmatic paths as feeders for the volcanism. The
557 period represented the initiation of the minor volcanic activity caused by major extension at a
558 local scale. The first volcanic activity commenced with regional stress induced by KTJ
559 tectonics at around 3 Ma. The swarm of parallel dykes in the southern part of KTJ,
560 particularly Özenç volcanic area (Fig. 2), show a stress field with σ_1 in a N–S direction and σ_3
561 in the E–W direction (Karaoğlu et al., in press). The strain direction associated with this dyke

562 emplacement confirms that volcanism was controlled by a NEE–SWW-trending zone of
563 weakness, particularly in the Özenç volcanic area and at the Turnadağ volcano.

564 **7. Conclusions**

565 We document numerical results on the mechanism of magma propagation paths under
566 a variety of tectonic loads in the crust. We particularly explore the relationship between
567 tectonics and magma propagation in the tectonic settings at the Karlıova Triple Junction
568 (KTJ) of Eastern Turkey. The interpretation of our numerical models suggests that Turnadağ
569 volcanism at the western part of the KTJ has been fed by a shallow magma chamber located
570 at about 8 km depth during E-W extension. Also, that the Varto caldera is fed by a shallow
571 magma chamber at a similar depth. More specifically, the numerical results show that if the
572 region was subject to an E-W-oriented compressional stress (σ_1), then magma propagation
573 and associated volcanic eruptions would most likely come to an end. Magma transfer
574 between the magma chambers of Varto volcano and Özenç volcanic area exhibits complex
575 stress interactions (Figs. 4, 5). The pattern of local stress changes from the eastern part of the
576 triple junction to the western part. Even though the Özenç volcanic area has experienced N-S-
577 directed compression, inversion tectonics encourage magma propagation through the crust.
578 Hence, loading during inversion tectonics dramatically changes the orientation of σ_1 and
579 affects magma propagation more than the individual extension or compression regimes. Local
580 stresses are dominated by a deep reservoir located at 15-18 km depth. It is this reservoir that
581 largely controls the potential of injected dykes reaching the surface and, additionally, the
582 locations of the eventual eruptions. Our three-dimensional models, simulating the complex
583 loading conditions at the KTJ triple junction, can be used (with suitable modifications) to
584 advance our understanding of triple junctions worldwide.

585 **Acknowledgements**

This study was supported by funds of the Yüzüncü Yıl Üniversitesi (Project No. 2014-MİM-B062). Özgür Karaoğlu is supported by The Scientific and Technological Research Council of Turkey (TUBITAK) International Postdoctoral Research Fellowship Programme. Thanks to the Editor, Tamsin Mather, and to the reviewers, Alessandro Tibaldi and Nicolas Le Corvec, for very helpful comments which greatly improved the paper.

605 **References**

606 Acocella, V., Funiciello, R., Marotta, E., Orsi, G., de Vita, S., 2004. The role of extensional
607 structures on experimental calderas and resurgence. J. Volcanol. Geoth. Res. 129 (1–
608 3), 199–217.

609 Acocella, V., Neri, M., 2009. Dike propagation in volcanic edifices: overview and possible
610 developments. Tectonophysics 471 (1), 67–77.

611 Aktug, B., Dikmen, Ü., Dogru, A., Ozener., H., 2013. Seismicity and strain accumulation
612 around Karlıova Triple Junction (Turkey). J. Geodyn. 67, 21–29.

613 Ambraseys, N.N., Zatopek, A., 1968. The Varto Ustukran earthquake of 19 August 1966. B.
614 Seismol Soc. Am. 58, 47–102.

615 Annen, C., Sparks, R.S.J., 2002. Effects of repetitive emplacement of basaltic intrusions on
616 the thermal evolution and melt generation in the crust. Earth Planet. Sci. Lett. 203,
617 937–955.

618 Amadei, B., Stephansson, O., 1997. Rock stress and its measurement. Chapman Hall, New
619 York.

620 Armijo, R., Meyer, B., Hubert-Ferrari, A., Barka, A.A., 1999. Propagation of the North
621 Anatolian Fault into the Northern Aegean: Timing and Kinematics. Geology 27, 267–
622 270.

623 Barka, A.A., 1992. The North Anatolian fault zone. Ann. Tecton. 6, 164–195.

624 Becerril, L.,Galindo, I., Gudmundsson, A., Morales, J.M., 2013. Depth of origin of magma in
625 eruptions. Sci. Rep. 3, 2762. http://doi.org/10.1038/srep02762.

626 Browning, J., Gudmundsson, A., 2015. Caldera faults capture and deflect inclined sheets: an
627 alternative mechanism of ring dike formation. B. Volcanol. 77 (1), 1-13.

628 Browning, J., Drymoni, K., Gudmundsson, A., 2015. Forecasting magma-chamber rupture at
629 Santorini Volcano, Greece. Sci. Rep. 5, 15785. http://doi.org/10.1038/srep15785.

630 Buket, E., Temel, A., 1998. Major-element, trace element, and Sr-Nd isotopic geochemistry
631 and genesis of Varto (Muş) volcanic rocks, Eastern Turkey. J. Volcanol. Geotherm.
632 Res. 85, 405–422.

633 Caricchi, L., Annen, C., Blundy, J., Simpson, G., Pinel, V., 2014. Frequency and magnitude
634 of volcanic eruptions controlled by magma injection and buoyancy. Nat. Geosci. 7
635 (2), 126–130.

636 Cavalié, O., Jónsson, S., 2014. Block-like plate movements in eastern Anatolia observed by
637 InSAR. Geophys. Res. Lett. 41, 26–31.

638 Chaussard, E., F. Amelung, F. 2014. Regional controls on magma ascent and storage in
639 volcanic arcs, Geochem. Geophys. Geosyst. 15, doi:10.1002/2013GC005216.

640 Chestler, S.R., Grosfils, E.B., 2013. Using numerical modeling to explore the origin of
641 intrusion patterns on Fernandina volcano, Galápagos Islands, Ecuador. Geophys Res.
642 Lett. 40 (17), 4565–4569.

643 Clemens, J.C., Mawer, C.K., 1992. Granitic magma transport by fracture propagation.
644 Tectonophysics 204, 339–360.

645 Daniels, K.A., Kavanagh, J.L., Menand, T., Stephen, J.S.R., 2012. The shapes of dikes:
646 Evidence for the influence of cooling and inelastic deformation. Geol. Soc. Am.
647 Bull. 124 (7-8), 1102–1112.

Deb, D., 2006. Finite Element Method, Concepts and Applications in Geomechanics. PHI Learning Private Limited, New Delhi.

Druitt, T.H., Sparks, R.S.J., 1984. On the formation of calderas during ignimbrite eruptions. Nature 310, 679–681.

Dzurisin, D., 2006. Volcano deformation: new geodetic monitoring techniques. Springer Verlag, Berlin.

Folch, A., Marti, J., 1998. The generation of overpressure in felsic magma chambers by replenishment. Earth Planet. Sci. Lett. 163 (1), 301–314.

Furlong, K.P., Schwartz, S.Y., 2004. Influence of the Mendocino triple junction on the tectonics of coastal California. Annu. Rev. Earth Planet. Sci. 32, 403–433.

Gaffney, E.S., Damjanac, B., 2006. Localization of volcanic activity: Topographic effects on dike propagation, eruption and conduit formation. Geophys. Res. Lett. 33, L14313, doi: 10.1029/2006GL026852.

Gaffney, E.S., Damjanac, B., Valentine, G.A., 2007. Localization of volcanic activity: 2. Effects of pre-existing structure. Earth Planet. Sci. Lett. 263 (3), 323–338.

Gerbault, M., 2012. Pressure conditions for shear and tensile failure around a circular magma chamber; insight from elasto-plastic modelling. Geol. Soc. (Lond.) Spec. Publ. 367 (1), 111–130.

Gerbault, M., Cappa, F., Hassani, R., 2012. Elasto-plastic and hydromechanical models of failure around an infinitely long magma chamber. Geochem. Geophys. Geosyst, 13 (3).

669 Geshi, N., Neri, M., 2014. Dynamic feeder dyke systems in basaltic volcanoes: the
670 exceptional example of the 1809 Etna eruption (Italy). Front. Earth Sci. 2: 13. doi:
671 10.3389/feart.2014.00013

672 Geyer, A., Marti, J., 2009. Stress fields controlling the formation of nested and overlapping
673 calderas: implications for the understanding of caldera unrest. J. Volcanol. Geoth.
674 Res. 181, 185–195.

675 Geyer, A., Folch, A., Martí, J., 2006. Relationship between caldera collapse and magma
676 chamber withdrawal: an experimental approach. J. Volcanol. Geoth. Res. 157 (4),
677 375–386.

678 Gregg, P.M., De Silva, S.L., Grosfils, E.B., Parmigiani, J.P., 2012. Catastrophic caldera-
679 forming eruptions: Thermomechanics and implications for eruption triggering and
680 maximum caldera dimensions on Earth. J. Volcanol. Geotherm. Res. 241, 1–12.

681 Gregg, P.M., de Silva, S.L., Grosfils, E.B., 2013. Thermomechanics of shallow magma
682 chamber pressurization: Implications for the assessment of ground deformation data at
683 active volcanoes. Earth Planet. Sci. Lett. 384, 100–108.

684 Gregg, P.M., Grosfils, E.B., de Silva, S.L., 2015. Catastrophic caldera-forming eruptions II:
685 The subordinate role of magma buoyancy as an eruption trigger. J. Volcanol.
686 Geotherm.Res. 305, 100–113.

687 Grosfils, E.B., 2007. Magma reservoir failure on the terrestrial planets: Assessing the
688 importance of gravitational loading in simple elastic models. J. Volcanol. Geotherm.
689 Res. 166 (2), 47–75.

690 Grosfils, E.B., McGovern, P.J., Gregg, P.M., Galgana, G.A., Hurwitz, D.M., Long, S.M.,
691 Chestler, S.R., 2015. Elastic models of magma reservoir mechanics: a key tool for
692 investigating planetary volcanism. Geol. Soc. (Lond.) Spec. Publ. 401 (1), 239–267.

693 Gudmundsson, A., 1990. Emplacement of dikes, sills and crustal magma chambers at
694 divergent plate boundaries. Tectonophysics 176, 257–275.

695 Gudmundsson, A., 2006. How local stresses control magma-chamber ruptures, dyke
696 injections, and eruptions in composite volcanoes. Earth-Sci. Rev. 79, 1–31.

697 Gudmundsson, A., 2011. Rock Fractures in Geological Processes. Cambridge University
698 Press, Cambridge.

699 Gudmundsson, A., 2012. Magma chambers: formation, local stresses, excess pressures, and
700 compartments, J. Volcanol. Geoth. Res. 237–238, 19–41.

701 Gudmundsson, A., 2015. Collapse-driven large eruptions. J. Volcanol. Geotherm. Res. 304,
702 1–10.

703 Gudmundsson, A., Philipp, S.L., 2006. How local stress fields prevent volcanic eruptions. J.
704 Volcanol. Geoth. Res. 158, 257–268.

705 Hubert-Ferrari, A., King, G., Woerd, J., Van der, Villa, I., Altunel, E., Armijo, R., 2009.
706 Long-term evolution of the North Anatolian Fault: new constraints from its eastern
707 termination. Geol. Soc. (Lond.) Spec. Publ. 311 (1), 133–154.

708 Hurwitz, D.M., Long, S.M., Grosfils, E.B., 2009. The characteristics of magma reservoir
709 failure beneath a volcanic edifice. J. Volcanol. Geotherm. Res. 188 (4), 379–394.

710 Hutton, D.H., 1988. Granite emplacement mechanisms and tectonic controls: inferences
711 from deformation studies. Transactions of the Royal Society of Edinburgh. Earth
712 Sci. 79 (2-3), 245–255.

713 Jarosinski, M., 2012. Compressive deformations and stress propagation in intracontinental
714 lithosphere: Finite element modelling along the Dinarides–East European Craton
715 profile. Tectonophysics 526–529, 24–41.

716 Karaoğlu, O., 2014. Tectonic controls on the Yamanlar volcano and Yuntdagi volcanic
717 region, western Turkey: implications for an incremental deformation. J. Volcanol.
718 Geoth. Res. 274, 16–33.

719 Karaoğlu, Ö., Sağlam-Selçuk, A., Gudmundsson, A. (in press). Tectonic controls on the
720 Karlıova Triple Junction (Turkey): implications for tectonic inversion and the
721 initiation of volcanism. Tectonophysics.

722 Kavanagh, J.L., Menand, T., Sparks, R.S.J., 2006. An experimental investigation of sill
723 formation and propagation in layered elastic media. Earth Planet. Sci. Lett. 245, 799–
724 813.

725 Le Corvec, N., Menand, T., Lindsay, J., 2013. Interaction of ascending magma with
726 pre-existing crustal fractures in monogenetic basaltic volcanism: an experimental
727 approach. J. Geophys. Res-Sol Ea. 118 (3), 968-984.

728 Le Corvec, N., McGovern, P.J., Grosfils, E.B., Galgana, G., 2015. Effects of crustal-scale
729 mechanical layering on magma chamber failure and magma propagation within the
730 Venusian lithosphere. J. Geophys. Res. 120 (7), 1279–1297.

731 Maccaferri, F., Rivalta, E., Keir, D., Acocella, V., 2014. Off-rift volcanism in rift zones
732 determined by crustal unloading. Nat. Geosci. 7 (4), 297–300.

733 Martí, J., Ablay, G.J., Redshaw, L.T., Sparks, R.S.J., 1994. Experimental studies of collapse
734 calderas. J. Geol. Soc. London 151, 919–929.

735 Martí, J., Geyer, A., Folch, A., Gottsmann, J., 2008. A review on collapse caldera modelling.
736 In: Gottsmann, J., Martí, J. (Eds.), Caldera Volcanism: Analysis, Modelling and
737 Response. Development in Volcanology. Elsevier, Amsterdam, vol.10, pp.233–283.

738 McClusky, S. et al., 2000. GPS constraints on plate motion and deformation in the eastern
739 Mediteranean: Implication for plate dynamics, J Geophys Res. 105, 5695–5719.

740 McKenzie, D., 1972. Active Tectonics of the Mediterranean Region, Geophys J Roy Astr S.
741 30, 109-185.

742 McKenzie, D.P., Parker, R.L., 1967. The North Pacific: an example of tectonics on a
743 sphere. Nature 216, 1276–1280.

744 Middlemost, E.A., 1997. Magmas, Rocks and Planetary Development: A Survey of
745 Magma/Igneous Rock Systems. Routledge, Oxford.

746 Ozener, H., E. Arpat, S. Ergintav, A. Dogru, R. Cakmak, B. Turgut, Dogan, U., 2010.
747 Kinematics of the Eastern Part of the North Anatolian Fault Zone, J Geodyn. 49 (3–
748 4), 141–150.

749 Pasquarè F., Tibaldi, A., 2007. Structure of a sheet-laccolith system revealing the interplay
750 between tectonic and magma stresses at Stardalur Volcano, Iceland. J. Volcanol.
751 Geotherm. Res. 161, 131–150.

752 Poidevin, J.L., 1998. Provenance studies of obsidian artefacts in Anatolia using the fission
753 track dating method, An overview, in L'Obsidienne au Proche et Moyen Orient, du
754 Volcan a` l'Outil, edited by A. Gourgaud, B. Gratuze, G. Poupeau, J.L. Poidevin and
755 M.C Cauvin, BAR International Series Hadrian Books, vol. 738, pp. 105–156.

756 Reilinger, R. et al., 2006. GPS constraints on continental deformation in the Africa–Arabia–
757 Eurasia continental collision zone and implications for the dynamics of plate
758 interactions, J Geophys Res. 111, B05411.

759 Sançar, C., Zabcı, C., Akyüz, H.S., Sunal, G., Villa, I.M., 2015. Distrubuted transpressive
760 continental deformation: The Varto Fault Zone, eastern Turkey, Tectonophysics 661,
761 99–111.

762 Sandvol, E., Turkelli, N., Zor, E., Gok, R., Bekler, T., Gurbuz, C., Seber, D., Barazangi, M.,
763 2003. Shear wave splitting in a young continent-continent collision: An example
764 from eastern Turkey. Geophys. Res. Lett. 30 (24), 8041–8059.

765 Sinton, J.M., Detrick, R.S., 1992. Mid-ocean magma chambers. J. Geophys. Res. 97, 197–
766 216.

767 Spence, D.A., Sharp, P.W., Turcotte, D.L., 1987. Buoyancy-driven crack propagation: a
768 mechanism for magma migration. J. Fluid Mech. 174, 135–153.

769 Şengör, A.M.C., Tüysüz, O., Imren, C., Sakınç, M., Eyidogan, H., Görür, N., Le Pichon, X.,
770 Rangin, C., 2004. The North Anatolian Fault: a new look, Annu. Rev. Earth Planet.
771 Sci. 33, 37–112.

772 Tan, O., Tapırdamaz, M.C., Yörük, A., 2008. The earthquake catalogues for Turkey. Turk. J.
773 Earth Sci. 17 (2), 405–418.

774 Tabatabaian, M., 2014. Comsol for Engineers. Mercury Learning and Information, Boston.

775 Tarhan, N., 1991. Hınıs–Varto–Karlıova (Erzurum–Muş–Bingöl) Dolayındaki Neojen
776 Volkanitlerinin Jeolojisi ve Petrolojisi. MTA Dergisi 113, 1–15 (in Turkish).

777 Tatar, O., Piper J.D.A., Gürsoy, H., Heimann, A., Koçbulut, F., 2004. Neotectonic
778 deformation in the transition zone between the Dead Sea Transform and the East
779 Anatolian Fault Zone, southern Turkey: a palaeomagnetic study of the Karasu Rift
780 Volcanism. Tectonophysics 385, 17–43.

781 Tibaldi A., 2015. Structure of volcano plumbing systems: A review of multi-parametric
782 effects. J. Volcanol. Geotherm. Res. 298, 85–135.

783 Tibaldi A., L. Vezzoli, F.A. Pasquarè, Rust, D., 2008. Strike-slip fault tectonics and the
784 emplacement of sheet-laccolith systems: The Thverfell case study (SW Iceland). J.
785 Struct. Geol. 30, 274–290.

786 Vigneresse, J.L., 1999. Intrusion level of granitic massifs along the Hercynian belt: balancing
787 the eroded crust. Tectonophysics 307, 277–295.

788 Williams, G.D., Powell, C.M., Cooper, M.A., 1989. Geometry and kinematics of inversion
789 tectonics. In: Cooper, M.A., Williams, G.D. (Eds.), Geol. Soc. (Lond.) Spec. Publ. 44., pp. 3–
790 15.

791 Zienkiewicz, O. C., 1979. The Finite Element Method. McGraw-Hill, New York, p. 787.

792

793

794

Figure captions

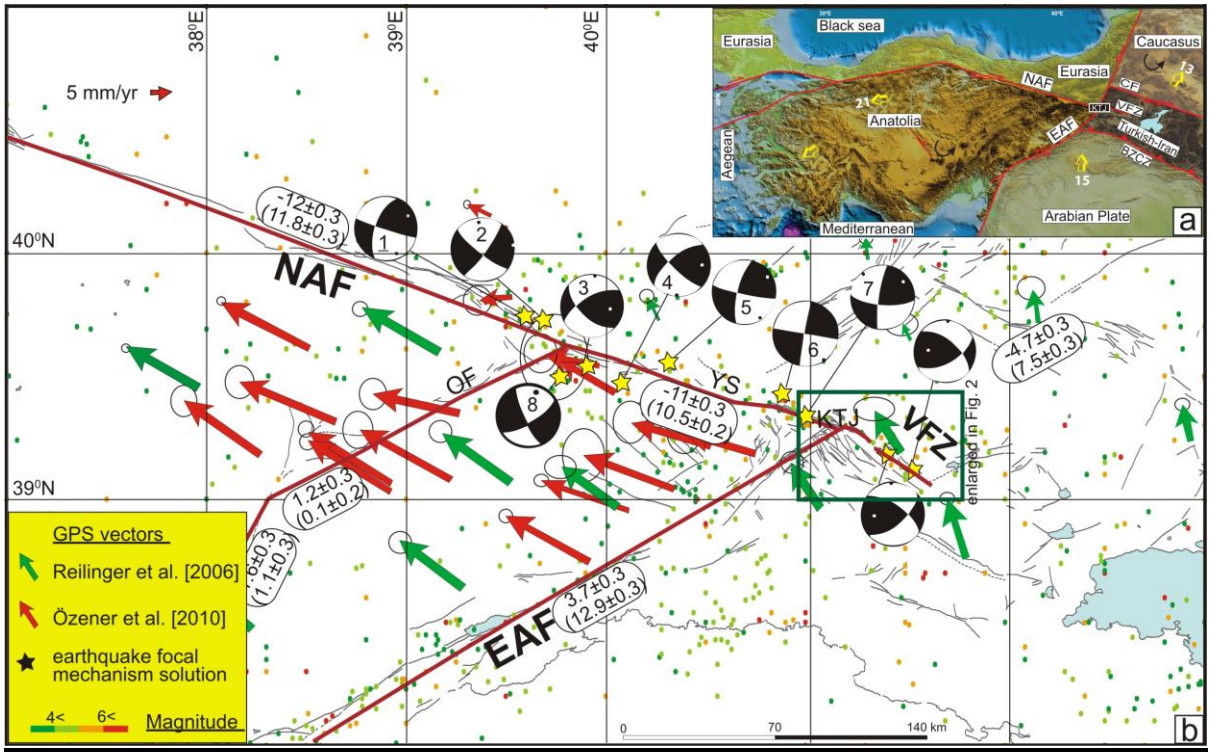

Figure 1. a) Major elements of crustal deformation in the eastern Mediterranean and Anatolia (Armijo et al., 1999). NAF: North Anatolian Fault, EAF: East Anatolian Fault, BZCZ: Bitlis-Zagros Collision Zone, CF: Çaldıran Fault, VFZ: Varto Fault Zone, YS: Yedisu Fault, KTJ: Karlıova Triple Junction; b) map showing GPS velocities with respect to Eurasia for 95% confidence ellipses (green vectors are Reilinger et al., 2006; red vectors are Ozener et al., 2010; and the focal mechanism solutions from Tan et al., 2008 for the study area). Numbers represent strike-slip component of the fault in mm/year, numbers within parentheses represent normal component of the fault, red lines are block boundaries (Aktug et al., 2013). Seismic data are from KOERİ (http://udim.koeri.boun.edu.tr/zeqdb/).

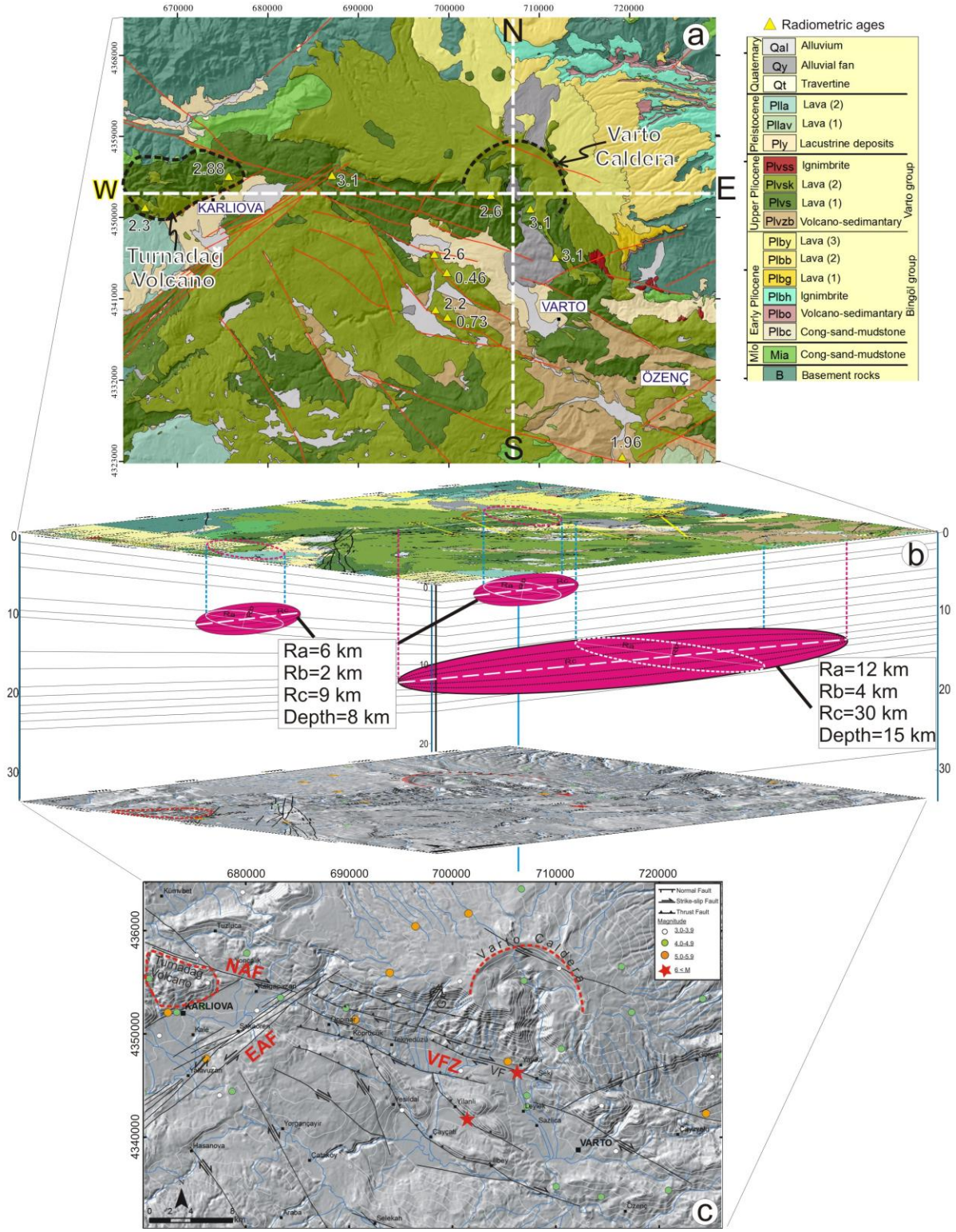

806

807 **Figure 2.** a) Geological map showing the main faults and seismicity around the Karlıova and

808 Varto region. Radiometric ages are given in Ma. Active faults are modified from Herece and

809 Akay (2003) and Sançar et al. (2015). b) Magma chambers on the block model using a

geological cross-section through the region and the physical parameters of the stratigraphy (Ra, Rb and Rc); c) Shaded relief basis map showing the main faults and seismicity around the Karlıova and Varto regions. Active faults are modified from Herece and Akay (2003) and Sançar et al. (2015). Seismicity data from KOERİ. NAF: North Anatolian Fault, EAF: East Anatolian Fault, KTJ: Karlıova Triple Junction, VFZ: Varto Fault Zone, VF: Varto Fault; GF: Güzeldere Fault.

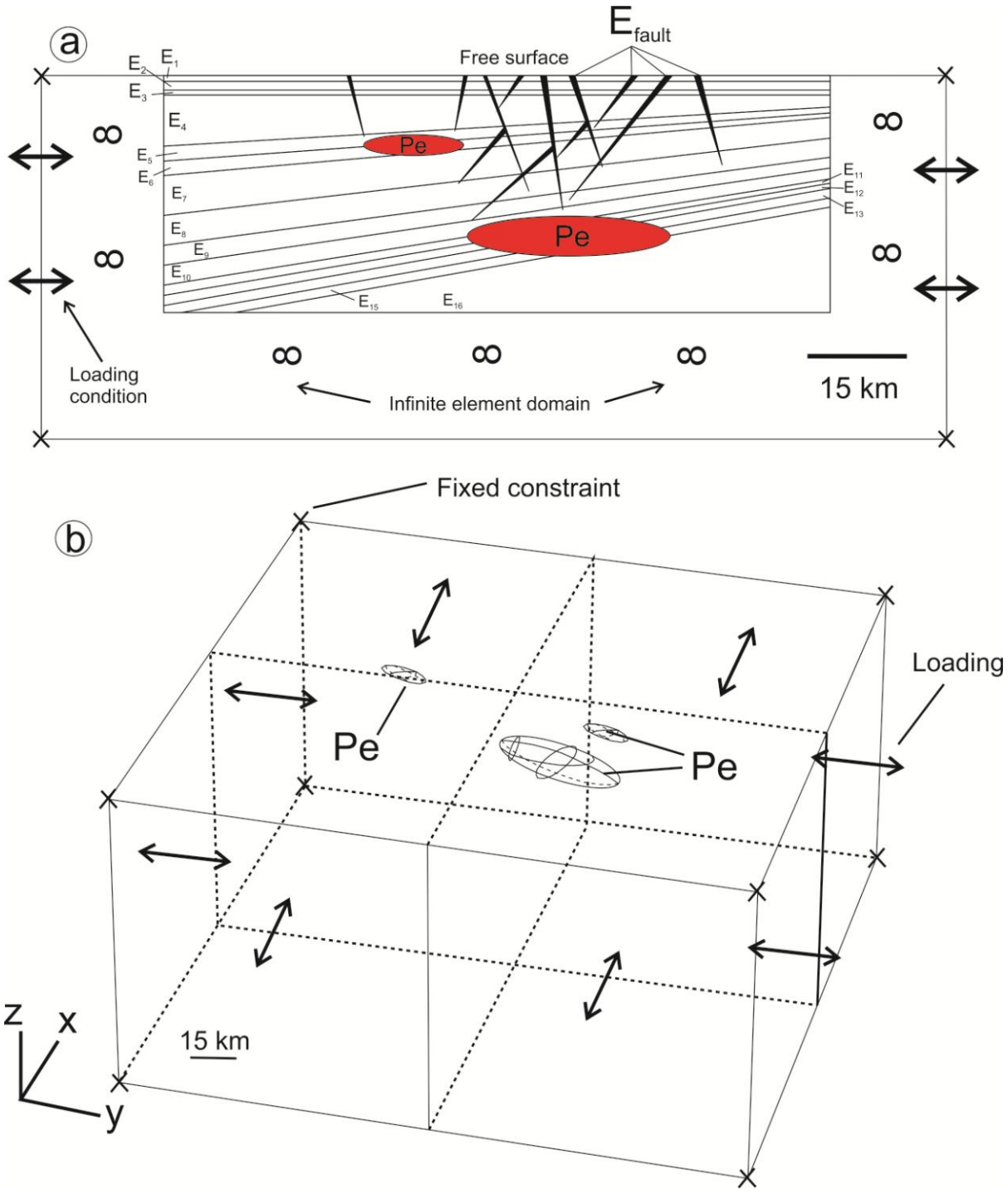

Figure 3. (a) 2-D and (b) 3-D numerical model setups. The 2-D example shown represents the geology of a N-S striking profile through Varto caldera to the East of the KTJ. All 2-D models are layered $E_{(1-16)}$ with each unit assigned a different value of Young's modulus. The dips of individual layers are based on field measurements. Faults (E_{fault}), shown as black polygons, are represented by zones of low stiffness and assigned Young's modulus of 0.1

GPa. Magma chambers, represented as cavities, are given an excess pressure of 5 to 15 MPa. Finally, boundary conditions such as extension or compression are assigned to the model edges. All 3-D models assume a homogeneous crustal segment with a Young's modulus of 40 GPa.

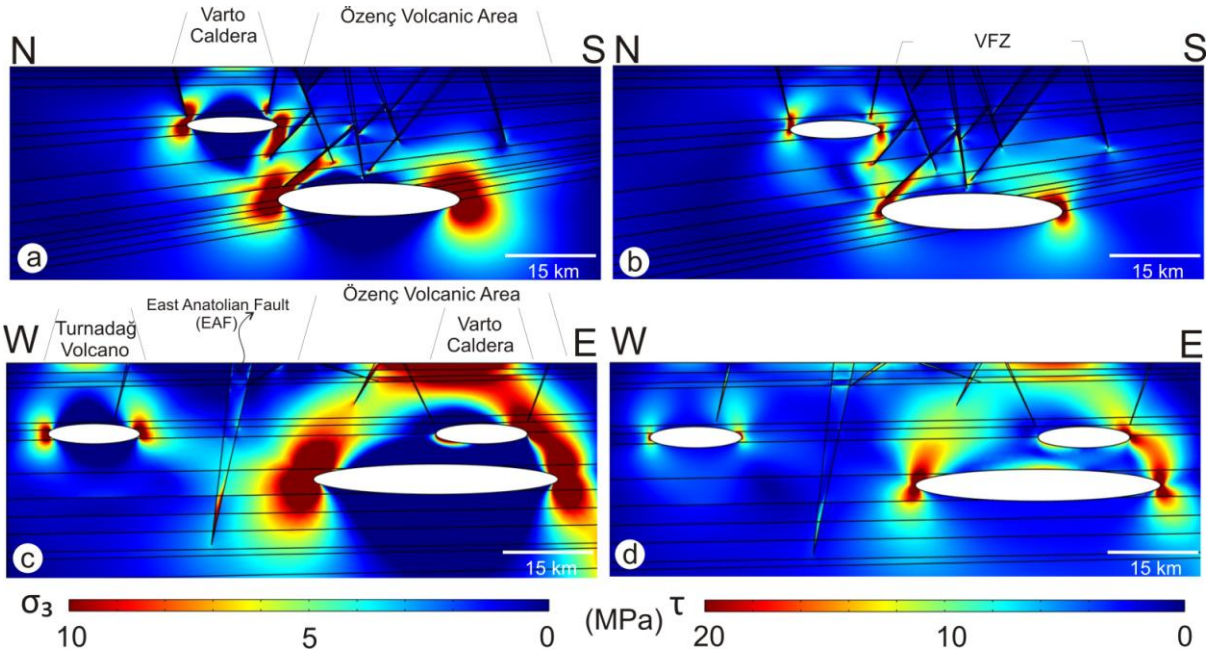

Figure 4. Modelled stresses induced by excess magmatic pressure based on the geologic setting along the Northern Anatolian fault region. Left: Magnitudes of the minimum principal compressive (maximum tensile) stress (σ_3). Right: Magnitude of von Mises shear stresses (τ) The excess magmatic pressure in each chamber is 5 MPa and is the only loading (no regional tectonic loading is applied here).

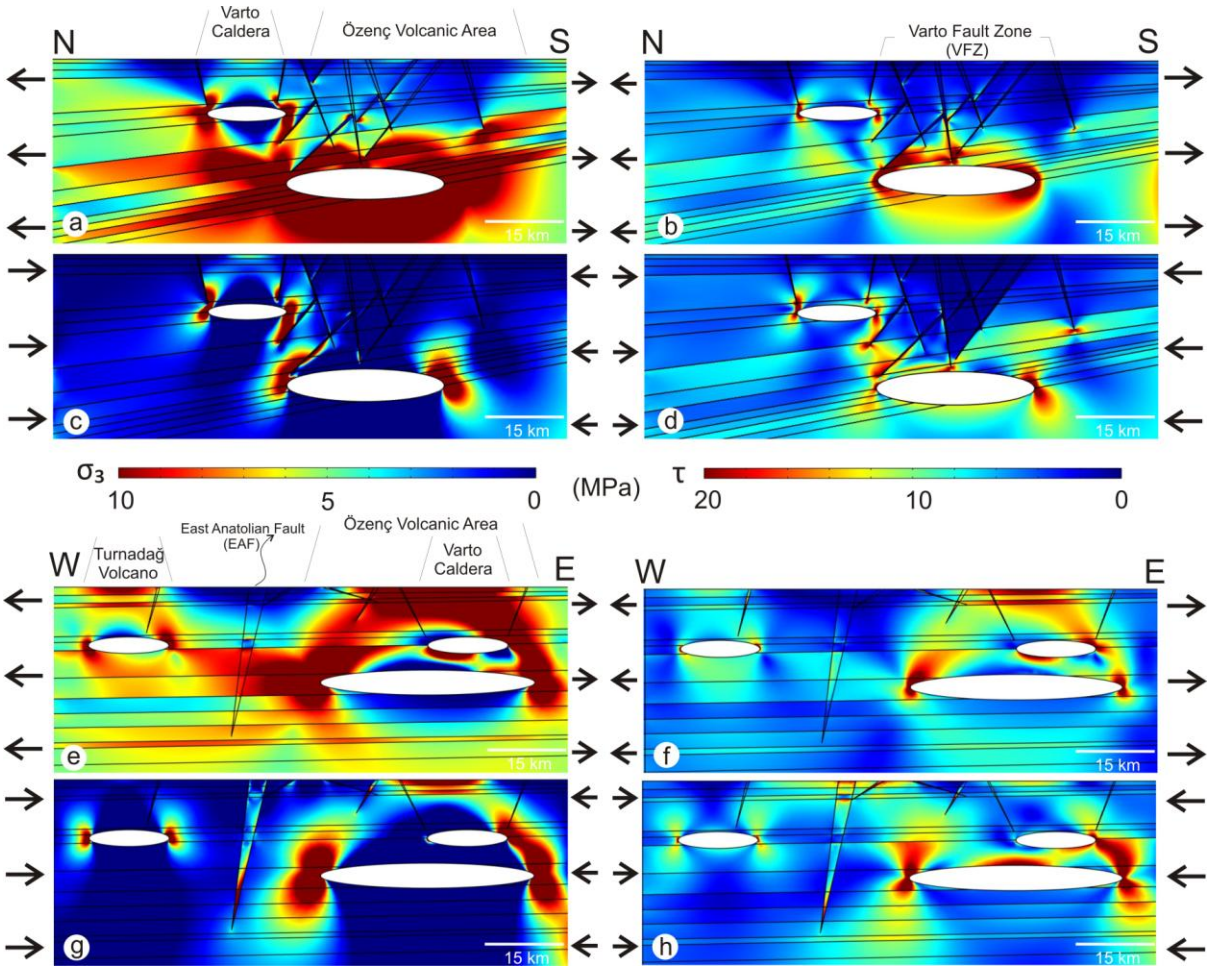

832

833 **Figure 5.** Modelled stresses resulting from regional tectonic extension (a-b and e-f) and
834 compression (c-d and g-h). Applied tensile and compressive boundary loads are 5 MPa and
835 excess magmatic pressure is 5 MPa in each chamber in all the models.

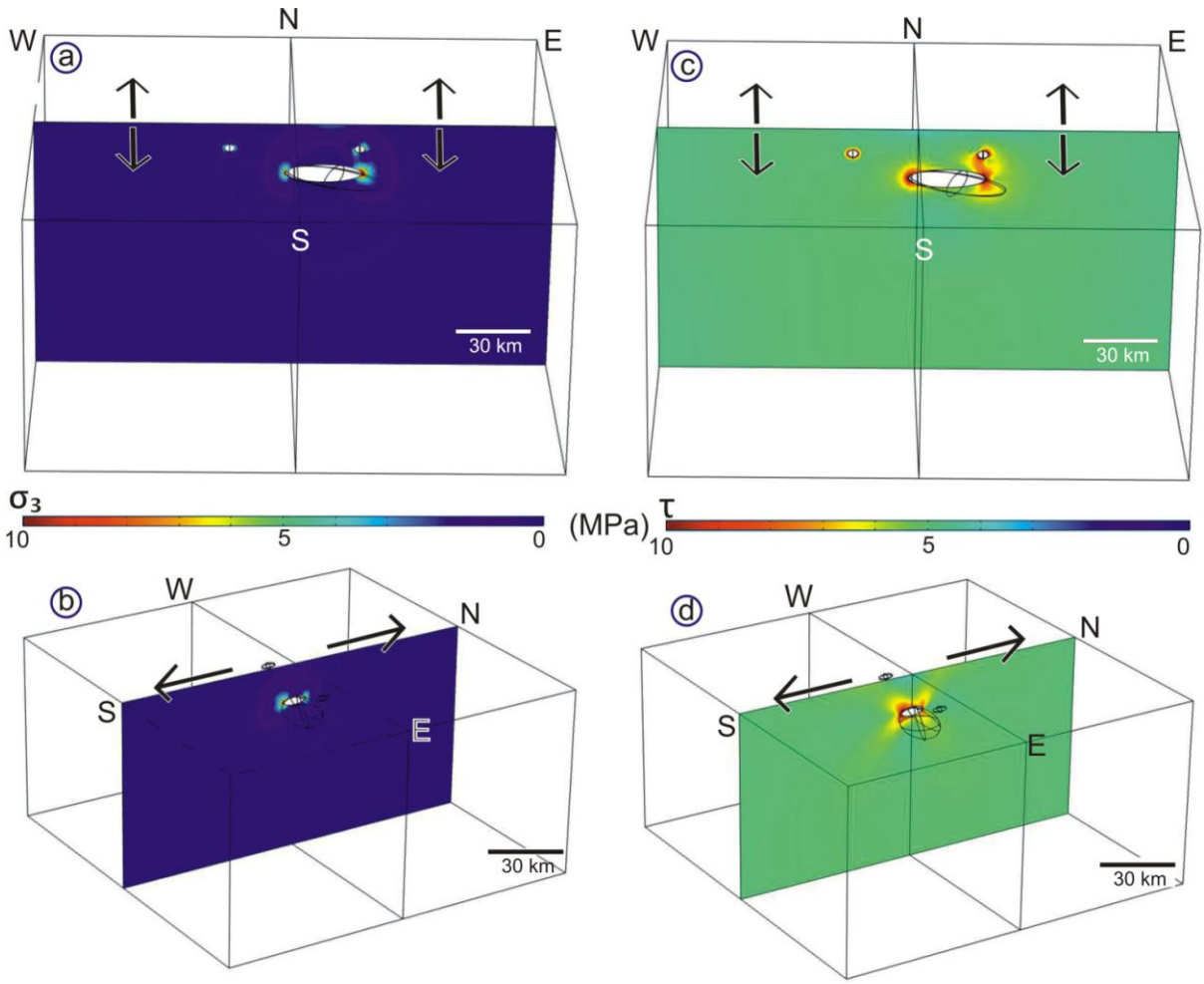

836

837 **Figure 6.** 3-D model showing the stresses resulting from tectonic extension from north to
838 south. Applied tensile and compressive boundary loads are 5 MPa and excess magma
839 pressure is 5 MPa in each chamber in all the models. a-b) Magnitudes of the minimum
840 principal compressive (maximum tensile) stress (σ_3), c-d) Magnitudes of von Mises shear
841 stress (τ).

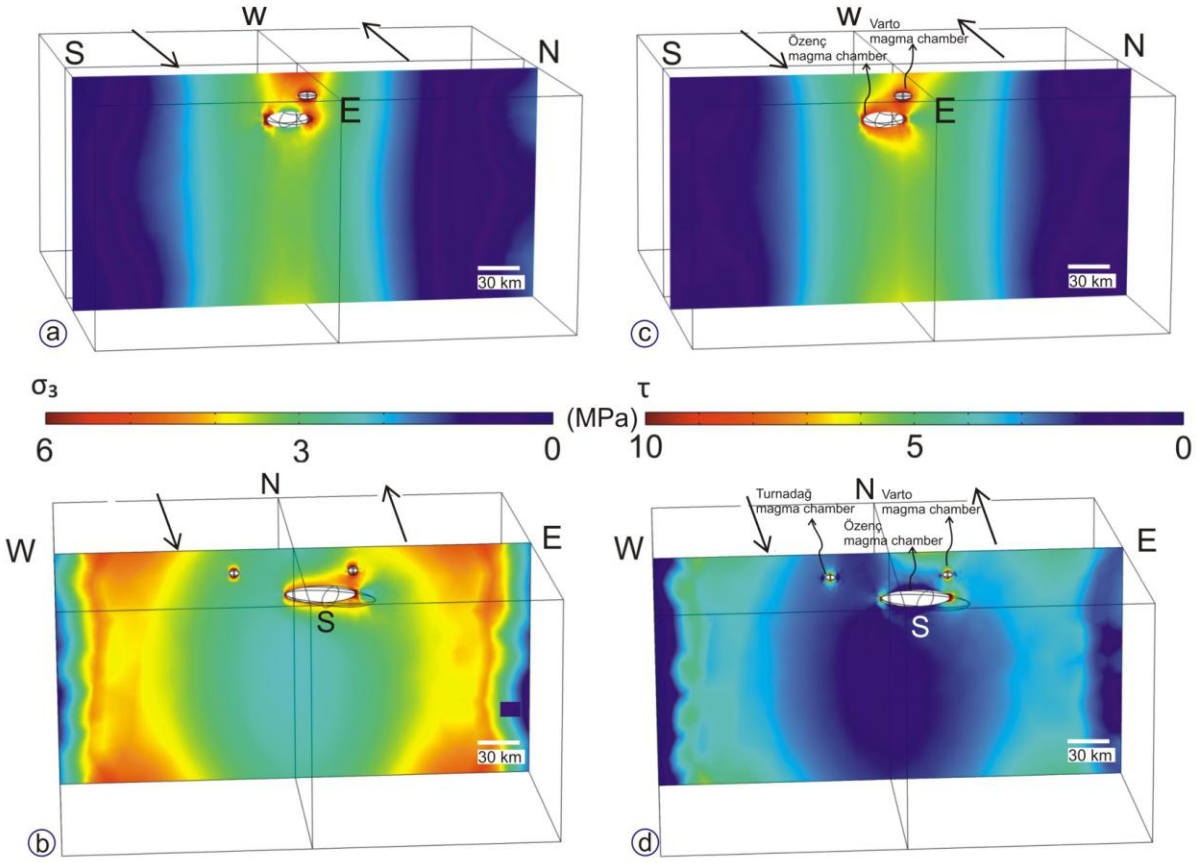

842

843 **Figure 7.** 3-D model showing the stresses resulting from an opposing boundary load
844 directions in a N-S direction. The eastern half of the model is subject to a 5 MPa load to the
845 north, and the western half of the model subject to the same load to the south. Excess
846 magmatic pressure is 5 MPa in each chamber in all models. a-b) Magnitudes of the minimum
847 principal compressive (maximum tensile) stress (σ_3). c-d) Magnitudes of von Mises shear
848 stress (τ).

849

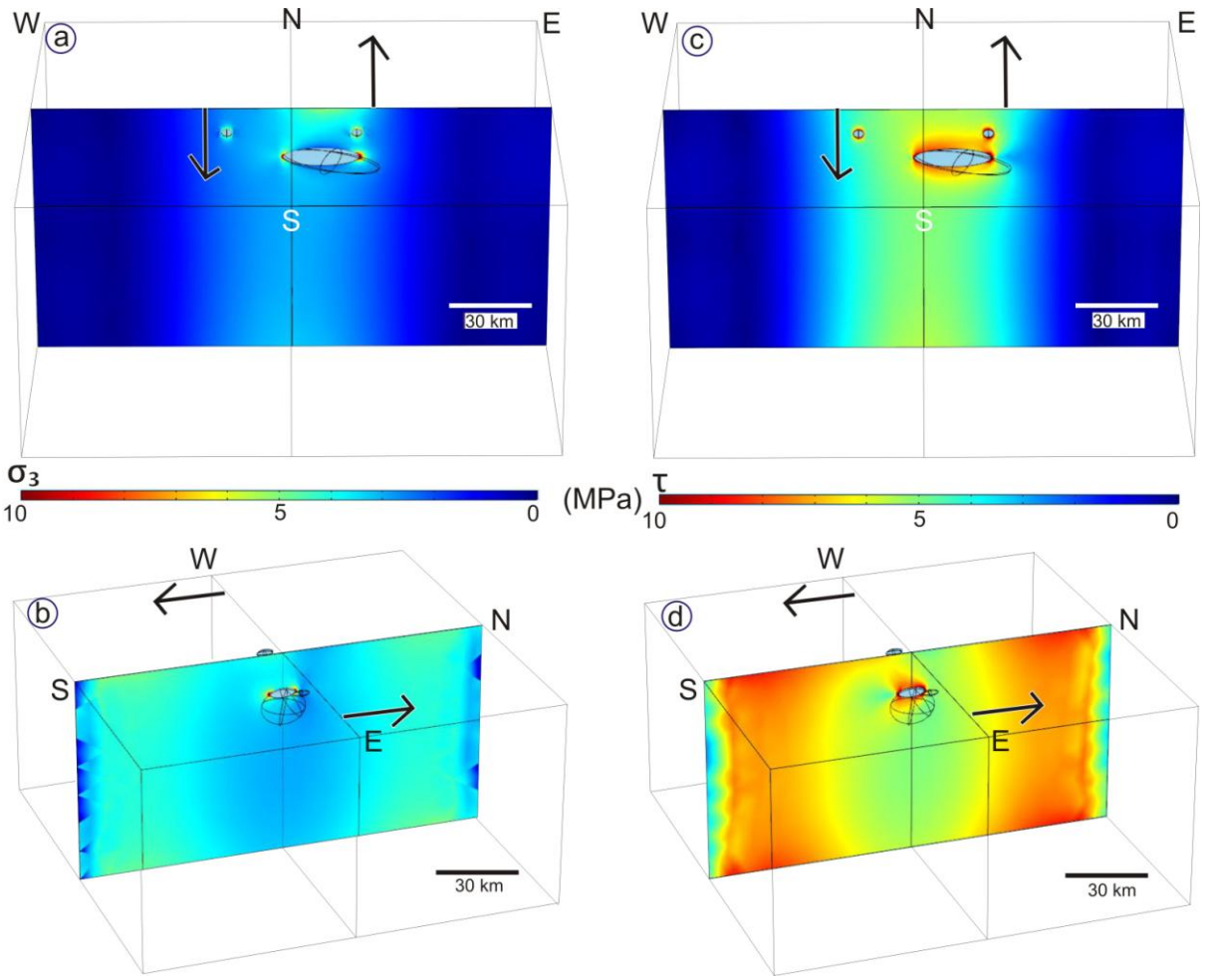

850

851 **Figure 8.** 3-D modelled stresses resulting from N−S-directed left-lateral tectonic shear
852 loading. Applied tensile and compressive boundary loads are 5 and excess magma pressure is
853 5 MPa in each chamber in all the models. a-b) Magnitudes of the minimum principal
854 compressive (maximum tensile) stress (σ_3). c-d) Magnitudes of von Mises shear stress (τ).

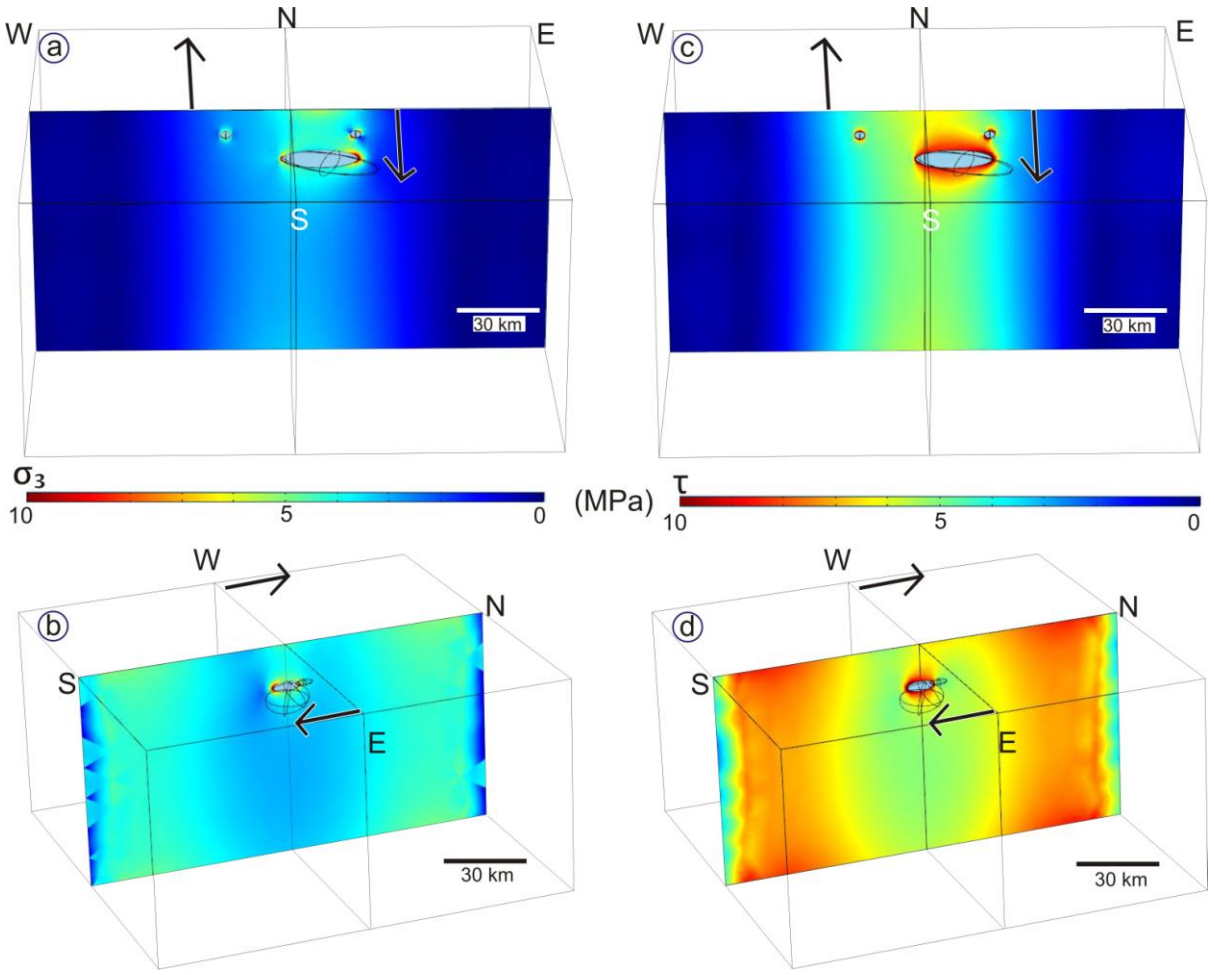

Figure 9. 3-D modelled stresses resulting from N−S-directed right-lateral tectonic shear loading. Applied tensile and compressive boundary loads are 5 and excess magmatic pressure is 5 MPa in each chamber in all models. a-b) Magnitudes of the minimum principal compressive (maximum tensile) stress (σ_3). c-d) Magnitudes of von Mises shear stress (τ).

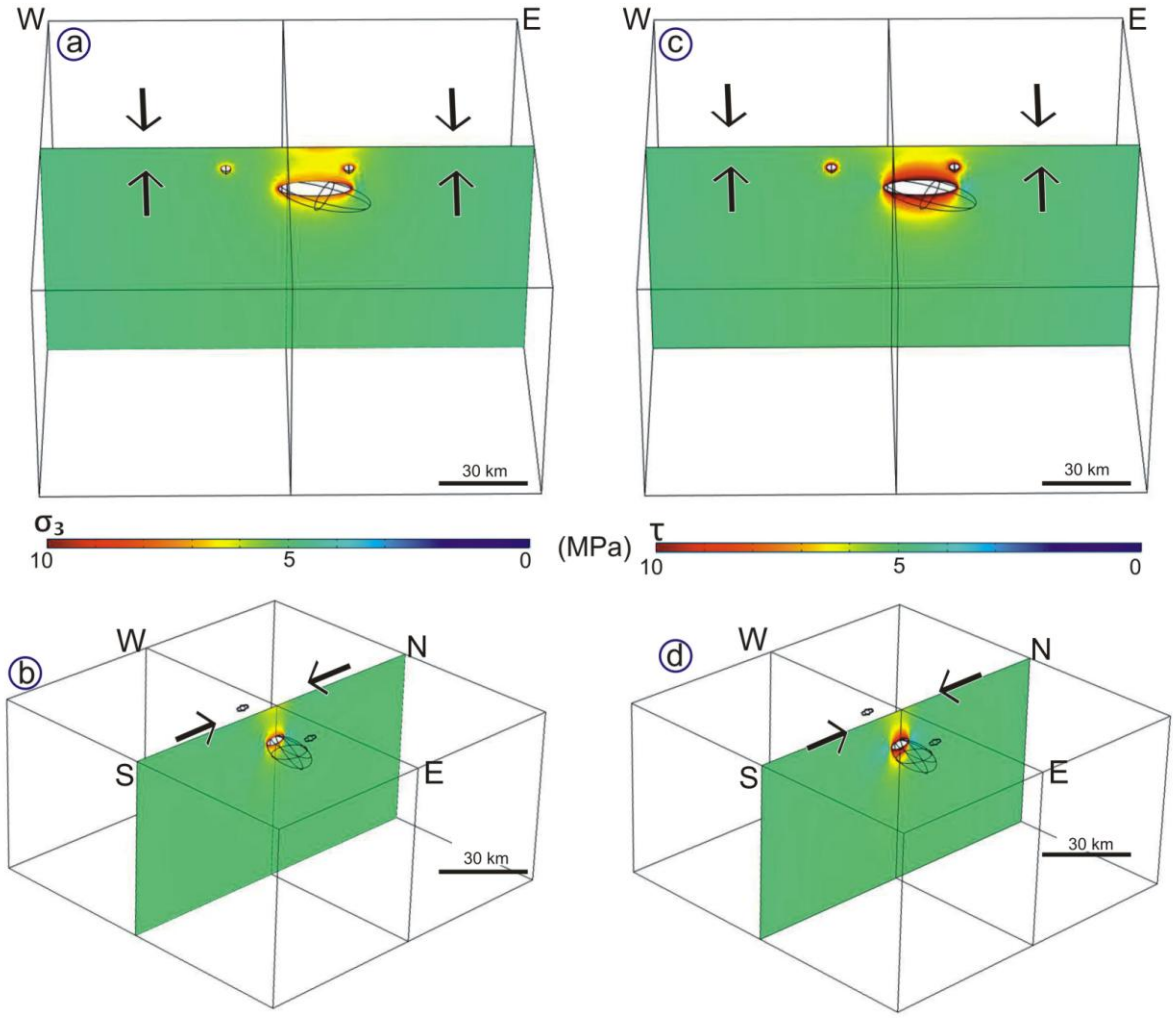

860

861 **Figure 10.** 3-D modelled stresses resulting from tectonic compression from north to south.
862 Applied tensile and compressive boundary loads are 5 and excess magmatic pressure is 5
863 MPa in each chamber in all the models. a-b) Magnitudes of the minimum principal
864 compressive (maximum tensile) stress (σ_3). c-d) Magnitudes of von Mises shear stress, σ_1-σ_3.

865